nature medicine

LETTERS

https://doi.org/10.1038/s41591-018-0006-x

Potent antitumor efficacy of anti-GD2 CAR T cells in H3-K27M$^+$ diffuse midline gliomas

Christopher W. Mount[1,2,3,12], Robbie G. Majzner[4,12], Shree Sundaresh[1], Evan P. Arnold[1], Meena Kadapakkam[4], Samuel Haile[4], Louai Labanieh[4,5], Esther Hulleman[6], Pamelyn J. Woo[1], Skyler P. Rietberg[4], Hannes Vogel[1,4,7,8], Michelle Monje[1,4,7,8,9,10*] and Crystal L. Mackall[4,9,11*]

Diffuse intrinsic pontine glioma (DIPG) and other diffuse midline gliomas (DMGs) with mutated histone H3 K27M (H3-K27M)[1–5] are aggressive and universally fatal pediatric brain cancers[6]. Chimeric antigen receptor (CAR)-expressing T cells have mediated impressive clinical activity in B cell malignancies[7–10], and recent results suggest benefit in central nervous system malignancies[11–13]. Here, we report that patient-derived H3-K27M-mutant glioma cell cultures exhibit uniform, high expression of the disialoganglioside GD2. Anti-GD2 CAR T cells incorporating a 4-1BBz costimulatory domain[14] demonstrated robust antigen-dependent cytokine generation and killing of DMG cells in vitro. In five independent patient-derived H3-K27M$^+$ DMG orthotopic xenograft models, systemic administration of GD2-targeted CAR T cells cleared engrafted tumors except for a small number of residual GD2^{lo} glioma cells. To date, GD2-targeted CAR T cells have been well tolerated in clinical trials[15–17]. Although GD2-targeted CAR T cell administration was tolerated in the majority of mice bearing orthotopic xenografts, peritumoral neuroinflammation during the acute phase of antitumor activity resulted in hydrocephalus that was lethal in a fraction of animals. Given the precarious neuroanatomical location of midline gliomas, careful monitoring and aggressive neurointensive care management will be required for human translation. With a cautious multidisciplinary clinical approach, GD2-targeted CAR T cell therapy for H3-K27M$^+$ diffuse gliomas of pons, thalamus and spinal cord could prove transformative for these lethal childhood cancers.

Immune checkpoint inhibitors mediate substantial benefit in adult cancers refractory to traditional therapies but have not yet demonstrated widespread benefit in sporadic childhood cancers, possibly owing to the paucity of neoantigens in these diseases[18]. In contrast, CAR T cell therapies have mediated highly potent effects in childhood B cell acute lymphoblastic leukemia (B-ALL). To identify potential targets for CAR T cell immunotherapy in DIPG, we screened cell surface antigens using an antibody array in patient-derived DIPG cultures (Fig. 1a and Supplementary Table 1). Considerable overlap between independent patient-derived cultures (Fig. 1b) suggests conservation of a core group of surface markers across patients with DIPG. From these common targets, we observed that the disialoganglioside GD2 was expressed at high levels on each of the four patient-derived DIPG cultures screened (Fig. 1a). Hit validation through flow cytometry in six H3-K27M$^+$ DIPG cultures confirmed uniform, high GD2 expression in all H3-K27M$^+$ DIPG cultures examined, including those with the *H3F3A* K27M mutation (SU-DIPG-6, SU-DIPG-13, SU-DIPG-17, SU-DIPG-25, SU-DIPG-29) and the less-common *HIST1H3B* K27M mutation (SU-DIPG-21)[2,19,20] (Fig. 1c). GD2 expression was far lower in two pediatric high-grade gliomas (pHGG) with wild-type H3 (H3-WT), including a case of H3-WT DIPG, than in the H3-K27M$^+$ DIPG cultures (Fig. 1c). To assess whether transcriptional perturbations resulting from the H3-K27M mutation might be linked to GD2 overexpression, we profiled the expression of genes encoding enzymes involved in ganglioside synthesis in patient-derived H3-K27M$^+$ DIPG and H3-WT pHGG cultures and found higher expression of genes encoding ganglioside synthesis enzymes upstream of GD2 in the H3-K27M$^+$ DIPG cultures (Supplementary Fig. 1). Double immunostaining of primary human DIPG tissue for H3-K27M to identify infiltrating malignant cells and for GD2 confirmed local expression of GD2 in the native tumor context (Fig. 1d).

GD2-targeting immunotherapies are currently under clinical and preclinical investigation in several diseases, including neuroblastoma, osteosarcoma and melanoma[14–17,21–24]. Unlike monoclonal antibodies, which do not efficiently cross the blood–brain barrier, activated T cells can infiltrate the central nervous system (CNS) following adoptive transfer[7,25]. We generated human GD2-targeted CAR T cells incorporating a 4-1BB costimulatory domain, CD8 transmembrane domain (TM), and CD3ζ[14] (GD2-CAR T cells; Fig. 1e) and observed substantial GD2-dependent killing at several effector to target (E:T) ratios (Fig. 1f) and cytokine generation (Fig. 1g) upon exposure to patient-derived DIPG cultures relative to control CD19-targeted CAR T cells incorporating 4-1BBz (CD19-CAR T cells). Notably, GD2-CAR T cells did not produce a substantial amount of cytokines or induce cell killing when exposed to the H3-WT,GD2$^-$ VUMC-DIPG10 patient-derived DIPG culture, providing evidence for therapeutic specificity of GD2-CAR T cells toward H3-K27M$^+$ DIPG. To further confirm the targeting specificity of GD2-CAR T cells, we used CRISPR–Cas9-mediated deletion of the gene encoding GD2 synthase (*B4GALNT1*) in patient-derived

[1]Department of Neurology, Stanford University School of Medicine, Stanford, CA, USA. [2]Medical Scientist Training Program, Stanford University, Stanford, CA, USA. [3]Neurosciences Program, Stanford University, Stanford, CA, USA. [4]Department of Pediatrics, Stanford University School of Medicine, Stanford, CA, USA. [5]Department of Bioengineering, Stanford University, Stanford, CA, USA. [6]Department of Pediatric Oncology, VU University Medical Center, Amsterdam, The Netherlands. [7]Department of Neurosurgery, Stanford University School of Medicine, Stanford, CA, USA. [8]Department of Pathology, Stanford University School of Medicine, Stanford, CA, USA. [9]Stanford Cancer Institute, Stanford University School of Medicine, Stanford, CA, USA. [10]Stanford Institute for Stem Cell and Regenerative Medicine, Stanford University School of Medicine, Stanford, CA, USA. [11]Department of Medicine, Stanford University School of Medicine, Stanford, CA, USA. [12]These authors contributed equally: Christopher W. Mount and Robbie G. Majzner.
*e-mail: mmonje@stanford.edu; cmackall@stanford.edu

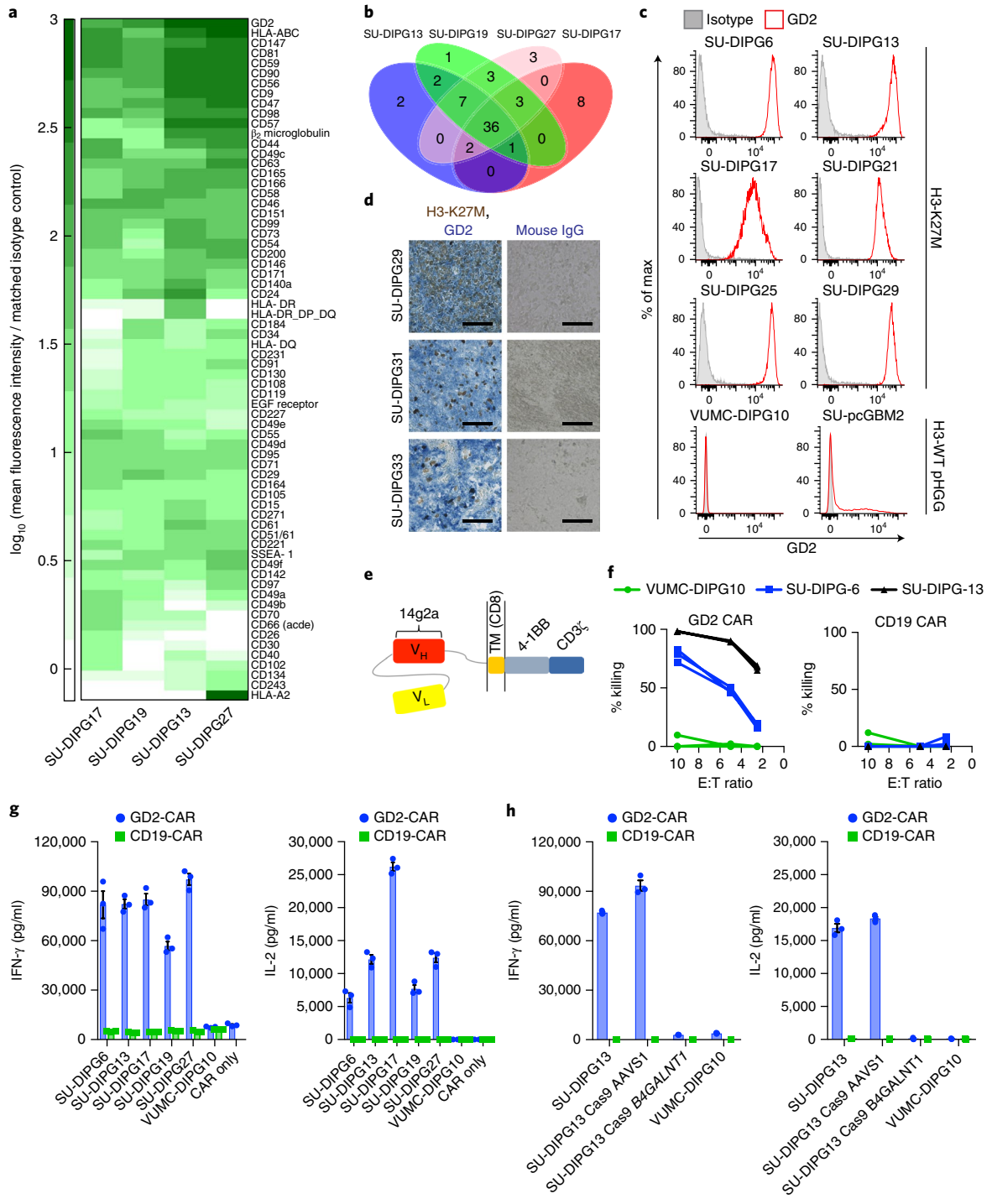

Fig. 1 | GD2 is a target for immunotherapy in DIPG. a, Top 68 antigens expressed on the cell surface in DIPG as determined using flow cytometry screening of a monoclonal antibody panel in patient-derived DIPG cell cultures (complete data are available in Supplementary Table 1). **b**, Assessment of hit overlap between screened cultures identified a total of 36 hits present at a mean fluorescence intensity (MFI) of at least ten times that of the isotype control in all screened cultures. **c**, Flow cytometry staining of H3-K27M$^+$ DIPGs revealing high, generally homogeneous GD2 expression in contrast to the H3-WT pediatric high-grade glioma cultures VUMC-DIPG10, diagnosed as a DIPG, and SU-pcGBM2, which arose in cerebral cortex. **d**, Double-staining immunohistochemistry of primary DIPG tumor specimens for mutant H3-K27M (brown) to identify tumor cells and the for GD2 (blue) showing extensive local GD2 expression in primary DIPGs. Scale bars, 100 μm. **e**, Schematic of the GD2.4-1BB.z-CAR used in functional experiments. V_H, variable heavy chain; V_L, variable light chain. **f**,**g**, GD2-CAR T cells, but not CD19-CAR T cells, mediate potent lysis (**f**) and produce high levels of IFN-γ (left) and IL-2 (right; **g**) following co-culture with GD2^{hi} DIPG cells expressing H3-K27M, but not GD2^{lo} or GD2$^-$ tumor cells expressing H3-WT. **h**, Levels of IFN-γ (left) or IL-2 (right) produced by GD2-CAR T cells following co-culture with the H3-K27M GD2$^-$ line that was generated using CRISPR–Cas9 to knock out GD2 synthase compared with levels produced by unmodified control cells or Cas9 targeting the control AAVS1 locus. Data are shown as mean ± s.e.m. In **f**–**h**, $n = 3$ independent samples; experiments in **c** and **d** were replicated twice.

DIPG cells to generate GD2-knockout DIPG cells (Supplementary Fig. 2). Loss of GD2 antigen expression eliminated cytokine production by the GD2-CAR T cells in comparison to DIPG cells that were untreated or electroporated with a control guide sequence targeting the AAVS1 locus (Fig. 1h). Although GD2 expression in healthy brain has been previously reported[26], no cases of substantial neurotoxicity have been reported in human trials of therapy with GD2-CAR T cells in which the targeting domain was derived from the same monoclonal antibody (14g2a) as used here [15–17]. Moreover, intrathecal and intraventricular administration of anti-GD2 antibody radioconjugates in subjects has been well tolerated in clinical trials[27,28]. Taken together, these findings indicate the specific reactivity of GD2-CAR T cells with H3-K27M$^+$ glioma cells.

To evaluate in vivo efficacy of GD2-CAR T cells against DIPG, we prepared orthotopic mouse xenografts of DIPG cultures derived from postmortem patient tissue. DIPG cultures were transduced with a luciferase-expressing construct to enable longitudinal monitoring of tumor burden. These xenograft models faithfully recapitulate the diffusely infiltrating histology of DIPG[29,30]. Mice were distributed according to tumor burden into equivalent treatment and control groups before receiving 1×10^7 GD2-CAR or CD19-CAR T cells via a single intravenous injection 7–8 weeks after establishment of pontine xenografts. Within 40 days post-treatment (DPT), marked reductions in tumor burden were observed across two independent cohorts of GD2-CAR T cell–treated mice bearing SU-DIPG6 xenografts[31] (Fig. 2a). Similar results were observed in a second patient-derived xenograft model, SU-DIPG13FL[30] (Fig. 2e). All GD2-CAR T cell–treated mice demonstrated complete tumor clearance as assessed through bioluminescence imaging (Supplementary Fig. 3). In contrast, no mice in the CD19-CAR T cell control group exhibited notable tumor regression. At 50 DPT, brains were excised, and immunostaining for the mutant histone H3-K27M—present in all engrafted tumor cells—revealed that GD2-CAR T cell–treated tumors had been largely eradicated (Fig. 2c,d,g–i). The small number of H3-K27M$^+$ tumor cells that remained after treatment did not express GD2 as determined through immunostaining (Supplementary Fig. 4). We hypothesize that the potency of GD2-CAR T cells in this model is driven by very high expression of the target antigen in H3-K27M-mutant DIPG, which was consistently higher than that in GD2$^+$ neuroblastoma and sarcoma cell lines (Supplementary Fig. 5). This study adds to the growing body of evidence suggesting that CAR T cells are more efficacious at high levels of target antigen expression[32,33].

In most patient-derived orthotopic DIPG xenograft models, lethality occurs many months after engraftment, limiting the ability to monitor survival benefit owing to development of xenogeneic graft versus host disease (GVHD) after treatment with human T cells[34]. We therefore used SU-DIPG-13P*, a model that exhibits a dense pattern of growth histologically[35] and is consistently lethal within 1 month. Substantial improvement in survival was seen in GD2-CAR T cell–treated mice compared with CD19-CAR T cell–treated controls (Fig. 3a). However, in one out of three independent cohorts, lethal toxicity occurred in several GD2-CAR T cell–treated NSG mice, whereas all GD2-CAR T cell–treated mice in the other cohorts survived to 50 DPT (Supplementary Fig. 6). GD2-CAR T cell–treated mice that survived the initial phase of glioma clearance returned to a visibly healthy state indistinguishable from that of untreated immunodeficient mice until the onset of GVHD symptoms 4+ weeks after CAR administration that invariably triggered endpoint criteria (Supplementary Fig. 7). Histologic analysis of the brains of GD2-CAR T cell–treated mice that reached endpoint revealed clearance of this high tumor burden, and surrounding neural tissues appeared grossly normal (Fig. 3b).

To better understand the etiology of treatment-related toxicity in these DIPG xenograft models, we examined the brains of GD2-CAR T cell–treated mice bearing SU-DIPG6 xenografts at 14 DPT (Fig. 3c). GD2-CAR T cell treatment was accompanied by a widespread inflammatory infiltrate involving brain parenchyma, meninges and ventricles that was most prominent in the brainstem. Ventriculomegaly was observed, consistent with hydrocephalus. We observed neurons that appeared histologically normal present throughout the pons, hippocampus and cortex of GD2-CAR T cell–treated mice with no evidence of neuronal cell killing or other tissue destruction in this model (Fig. 3c). Thus, neuropathological evaluation indicates that the toxicity described above results from brainstem inflammation and hydrocephalus due to fourth ventricular compression during the tumor-clearing interval and not from on-target, off-tumor toxicity of GD2-CAR T cells.

To visualize CAR T cell infiltration into the parenchyma and tumor, we generated GD2-4-1BBz-mCherry and CD19-4-1BBz-mCherry fusion constructs (Fig. 3d). By 7 DPT, GD2-CAR T cells were extensively distributed throughout the leptomeninges of treated mice, leptomeningeal tumor had been largely eradicated, and few mCherry$^+$ cells were present within brain parenchyma (Fig. 3h and Supplementary Fig. 8). By 14 DPT, mCherry$^+$ GD2-CAR T cells had widely infiltrated parenchyma, and numerous foci of ionized calcium-binding adapter molecule 1 (IBA1)$^+$ macrophages (Fig. 3e) along with extensive apoptotic cleaved caspase-3$^+$ cells (Fig. 3f) were present in the xenografted site. Notably, very few cleaved caspase-3$^+$ apoptotic cells were also NeuN$^+$ neurons as determined through double immunostaining (ten total apoptotic neurons were identified across four mice; Fig. 3g and Supplementary Fig. 9). By 21 DPT, mCherry$^+$ GD2-CAR T cells remained present throughout the CNS, whereas few CD19-CAR T cells had infiltrated the parenchyma (Supplementary Fig. 8). This supports a model in which intravenously administered GD2-CAR T cells enter through the meningeal lymphatic system[36] and then subsequently infiltrate brain parenchyma, although the mechanism of CAR T cell trafficking to the tumor remains to be defined. Given that resolution of tumor clearance and ventriculomegaly temporally coincide in treated mice, it is likely that antigen-specific antitumor activity, rather than on-target, off-tumor cell killing, precipitates neuroinflammation and edema during active tumoricidal activity that results in hydrocephalus. Understanding systemic and microenvironmental mechanisms that contribute to the resolution of acute CAR T cell–induced neuroinflammation is a critical area of future study that may be best addressed in immunocompetent models.

Recent World Health Organization (WHO) criteria place DIPG within a larger classification of diffuse midline gliomas (DMG) expressing mutant H3-K27M (Fig. 4a)[37]. In patient-derived cultures of pediatric H3-K27M thalamic (QCTB-R059, derived from resection)[4] and spinal cord (SU-pSCG1, derived postmortem) DMGs, GD2 is also highly and uniformly expressed (Fig. 4b) and triggers interferon (IFN)-γ and IL-2 production by GD2-CAR T cells (Fig. 4c). Although these data might reasonably predict similar efficacy of GD2-CAR T cells in these midline H3-K27M gliomas, we reasoned that the neuroanatomical site of disease could impact outcomes of CAR T cell therapy. To explore in vivo GD2-CAR T cell efficacy in these H3-K27M DMGs, we generated patient-derived orthotopic xenograft models of spinal cord (SU-pSCG1) and thalamic (QCTB-R059) glioma. When engrafted in the medulla to avoid the paralysis induced by injection into the spinal cord, widespread SU-pSCG1 growth was observed throughout the CNS (Fig. 4d). Systemic administration of GD2-CAR T cells achieved potent and lasting tumor clearing in this model of glioma xenograft in spinal cord, assessed both through longitudinal bioluminescence imaging (Fig. 4d,e) and endpoint histology; approximately 16 residual H3-K27M$^+$ cells per mouse remained across the sampled tissue volume of three GD2-CAR T cell–treated mice (Fig. 4f,g). No mice from this cohort died during the tumor-clearing phase.

To evaluate efficacy in H3-K27M thalamic glioma, we engrafted QCTB-R059 cells orthotopically in the thalamus (Fig. 4h). Tumor

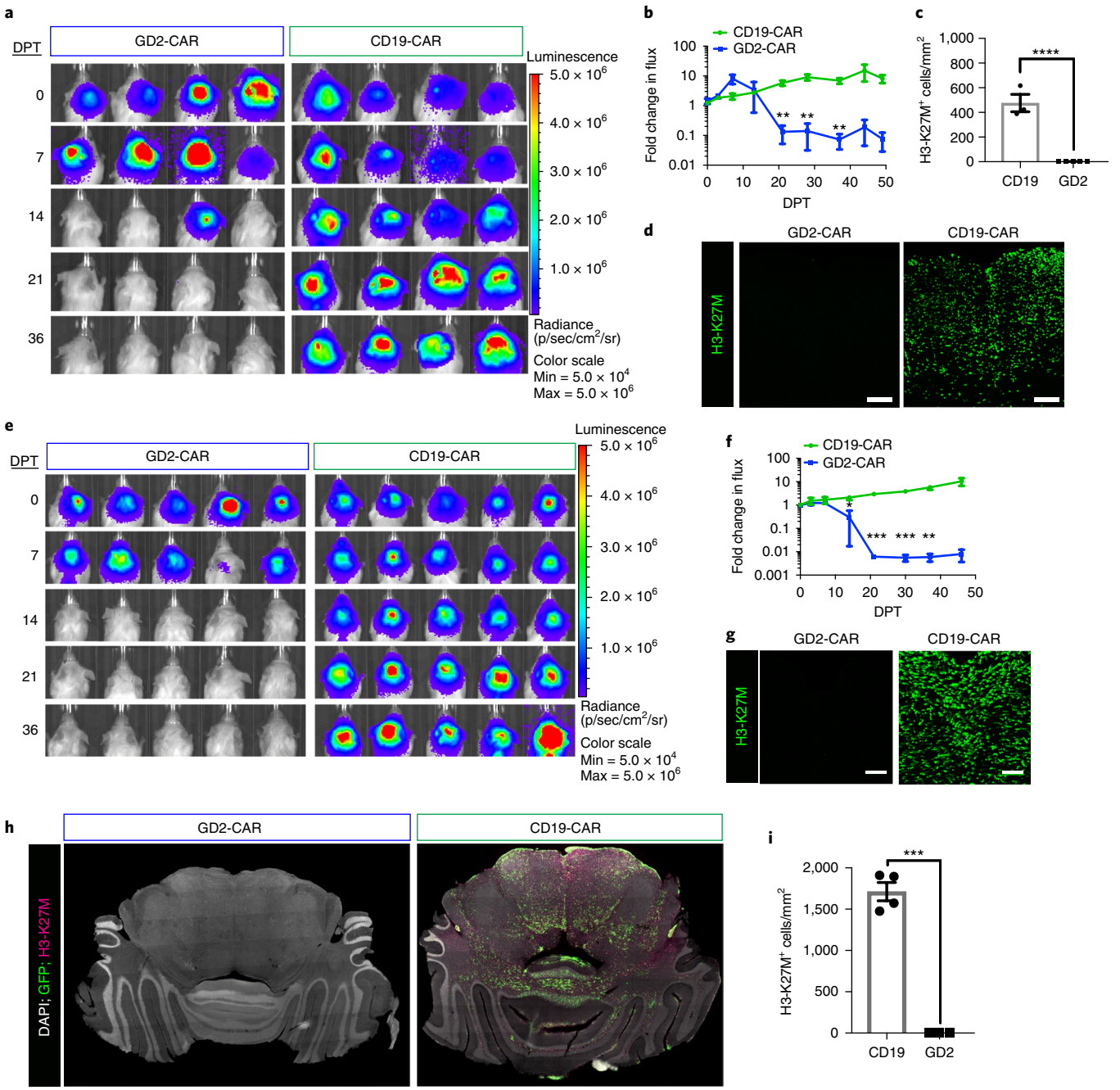

Fig. 2 | GD2-CAR T cells mediate a potent and lasting antitumor response in DIPG orthotopic xenografts. a, Representative bioluminescence imaging of NSG mice xenografted with luciferase-expressing SU-DIPG6 into the pons (color map for all images: radiance, minimum = 5×10^4, max = 5×10^6) and infused intravenously with 1×10^7 GD2-CAR or CD19-CAR T cells as designated. Each column represents one mouse; each row represents the time point at which imaging was performed. Antitumor response was observed between 14 and 28 DPT in GD2-CAR T cell–treated mice. **b**, Change in tumor burden in SU-DIPG6-engrafted GD2-CAR T cell– versus CD19-CAR T cell–treated mice ($n = 10$ and 11 mice, respectively) over time expressed as fold change in flux. **c**, Quantification of H3-K27M$^+$ tumor cell density within infiltrated brainstem regions of SU-DIPG6-engrafted GD2-CAR T cell– versus CD19-CAR T cell–treated mice ($n = 5$ and 3 mice, respectively). Within GD2-CAR T cell–treated SU-DIPG6 xenografts, we identified approximately 36 H3-K27M$^+$ cells remaining per mouse in the sampled tissue volume, whereas there were approximately 18,596 cells per mouse in the sampled tissue volume of CD19-CAR T cell–treated controls. **d**, Representative immunofluorescence confocal microscopy of CD19-CAR T cell– and GD2-CAR T cell–treated SU-DIPG6 tumors staining for the mutant histone H3-K27M (green). Scale bars, 100 μm. **e**,**f**, GD2-CAR activity in a second patient-derived orthotopic xenograft model of DIPG, SU-DIPG13FL. Bioluminescent imaging over time as above (**e**), and tumor burden over time expressed as fold change in flux ($n = 13$ GD2-CAR T cell– and 14 CD19-CAR T cell–treated mice; **f**). **g**, Representative immunofluorescent confocal microscopy of SU-DIPG13FL xenografts treated with CD19- or GD2-CAR T cells reveals clearance of H3-K27M$^+$ tumor cells. Scale bars, 100 μm. **h**, Tiled immunofluorescence images across brainstem and cerebellum regions engrafted with H3-K27M$^+$GFP$^+$ glioma cells. **i**, Quantification of H3-K27M$^+$ tumor cell density within infiltrated brainstem regions of SU-DIPG13FL ($n = 4$ GD2-CAR T cell– and 3 CD19-CAR T cell–treated mice). In SU-DIPG13FL xenografts, approximately 32 total H3-K27M$^+$ cells remained in the sampled tissue volume of each GD2-CAR T-cell treated mouse, compared to approximately 31,953 cells per mouse in the sampled tissue volume of CD19-CAR T cell–treated controls. Data are shown as mean ± s.e.m. $^{****}P < 0.0001$, $^{***}P < 0.001$, $^{**}P < 0.01$, $^{*}P < 0.05$ determined through unpaired two-tailed Student's *t*-test, with Holm–Sidak correction for multiple comparisons applied for bioluminescence imaging data. Experiments were replicated in two independent cohorts of mice. In all panels, *n* values indicate independent mice.

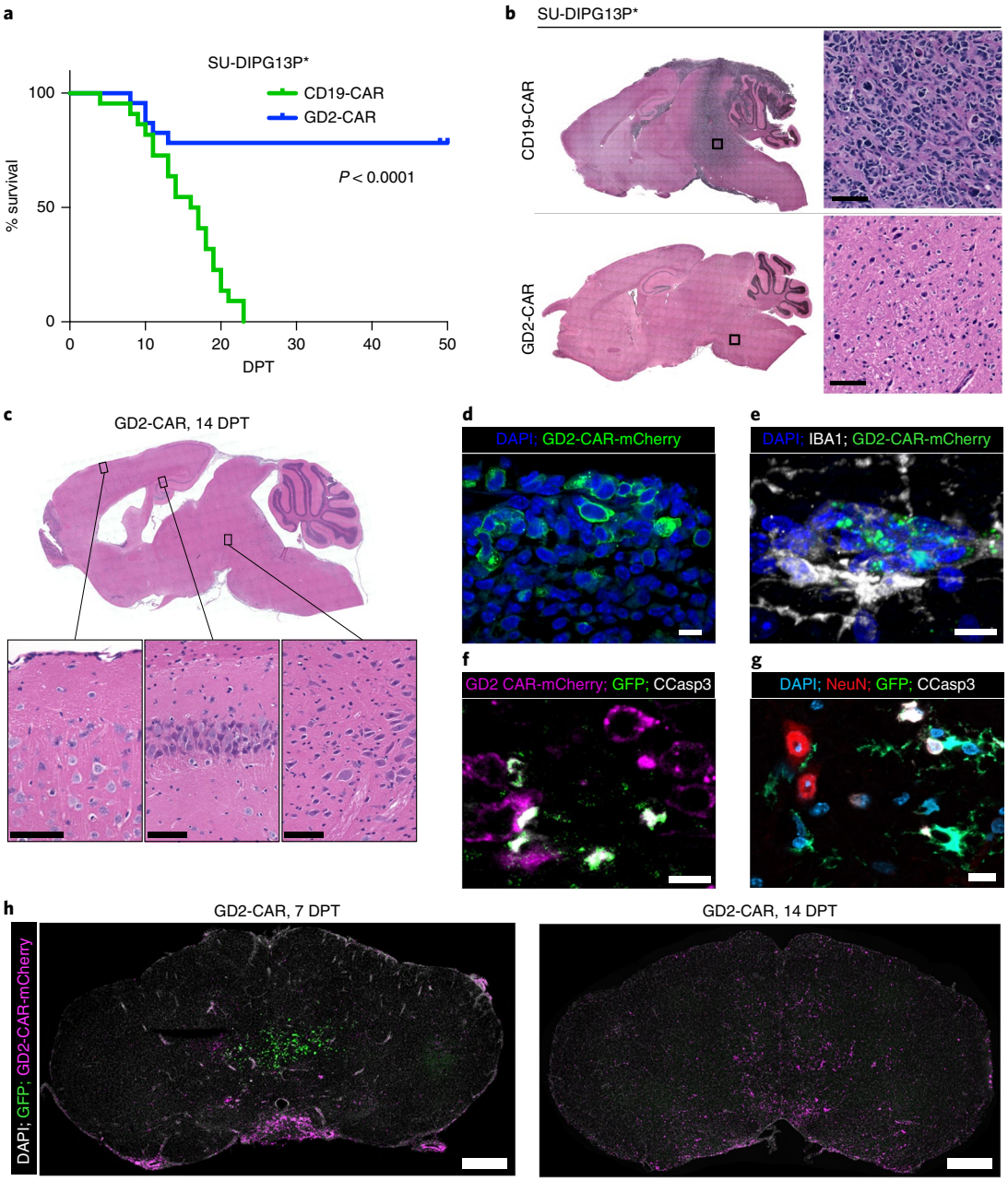

Fig. 3 | GD2-CAR T cell therapy improves survival in mice with DIPG orthotopic xenografts. a, Survival analysis of GD2-CAR T cell–treated orthotopic xenografts in SU-DIPG-13P*, a particularly aggressive patient-derived xenograft mouse model of DIPG that is lethal within 1 month of engraftment, showing a robust improvement in survival of GD2-CAR T cell–treated mice ($n = 22$ and 23 mice, respectively, across 3 independent cohorts (Supplementary Fig. 6); $P < 0.0001$; log-rank (Mantel–Cox) test). **b**, H&E staining of SU-DIPG13P* xenografts at 50 DPT demonstrates clearance by GD2-CAR T cells of highly infiltrative parenchymal tumor observed throughout the brain in CD19-CAR T cell–treated controls and normal gross tissue architecture. Scale bars, 100 μm. **c**, H&E staining of SU-DIPG6 GD2-CAR T cell–treated xenografts analyzed at 14 DPT showing ventriculomegaly but neurons that appear histologically normal in cortex, hippocampus and brainstem (left, middle and right inset images, respectively). Scale bars, 100 μm. **d**, Fluorescence microscopy of DPT7 SU-DIPG13FL xenografts reveals intravenously administered GD2-CAR-mCherry T cells infiltrating the engrafted tumor. Scale bar, 10 μm. **e**, Representative image of infiltrating GD2-CAR-mCherry T cells at 14 DPT in a SU-DIPG13FL xenografted medulla demonstrates spatial association with IBA1$^+$ macrophages. Scale bar, 10 μm. **f**, Representative image of GD2-CAR-mCherry T cell–mediated killing of tumor cells with apoptosis of GFP$^+$ tumor cells as evidenced by colocalization with cleaved caspase-3 (CCasp3)$^+$ cells. Scale bar, 10 μm. **g**, Representative image at 7 DPT showing tumoricidal activity occurring in proximity to nonapoptotic NeuN$^+$ neurons in the xenografted pons (Supplementary Fig. 9). Scale bar, 10 μm. **h**, Representative images of GD2-CAR-mCherry T cells infiltrating the parenchyma of SU-DIPG13FL xenografts during the period of acute antitumor activity (Supplementary Fig. 8). Scale bars, 500 μm. Experiments in **b**–**h** were repeated twice.

clearance was observed in this model (Fig. 4h,i and Supplementary Fig. 10) on a similar time scale as that observed for the DIPG and spinal cord tumors discussed above. However, substantial toxicity occurred in GD2-CAR T cell–treated mice during the period of maximal therapeutic effect (Fig. 4k). The results are reminiscent of 'pseudoprogression', a process that is well described following immunotherapy with checkpoint inhibitors[38], and highlight the danger of a robust immunotherapeutic response and subsequent

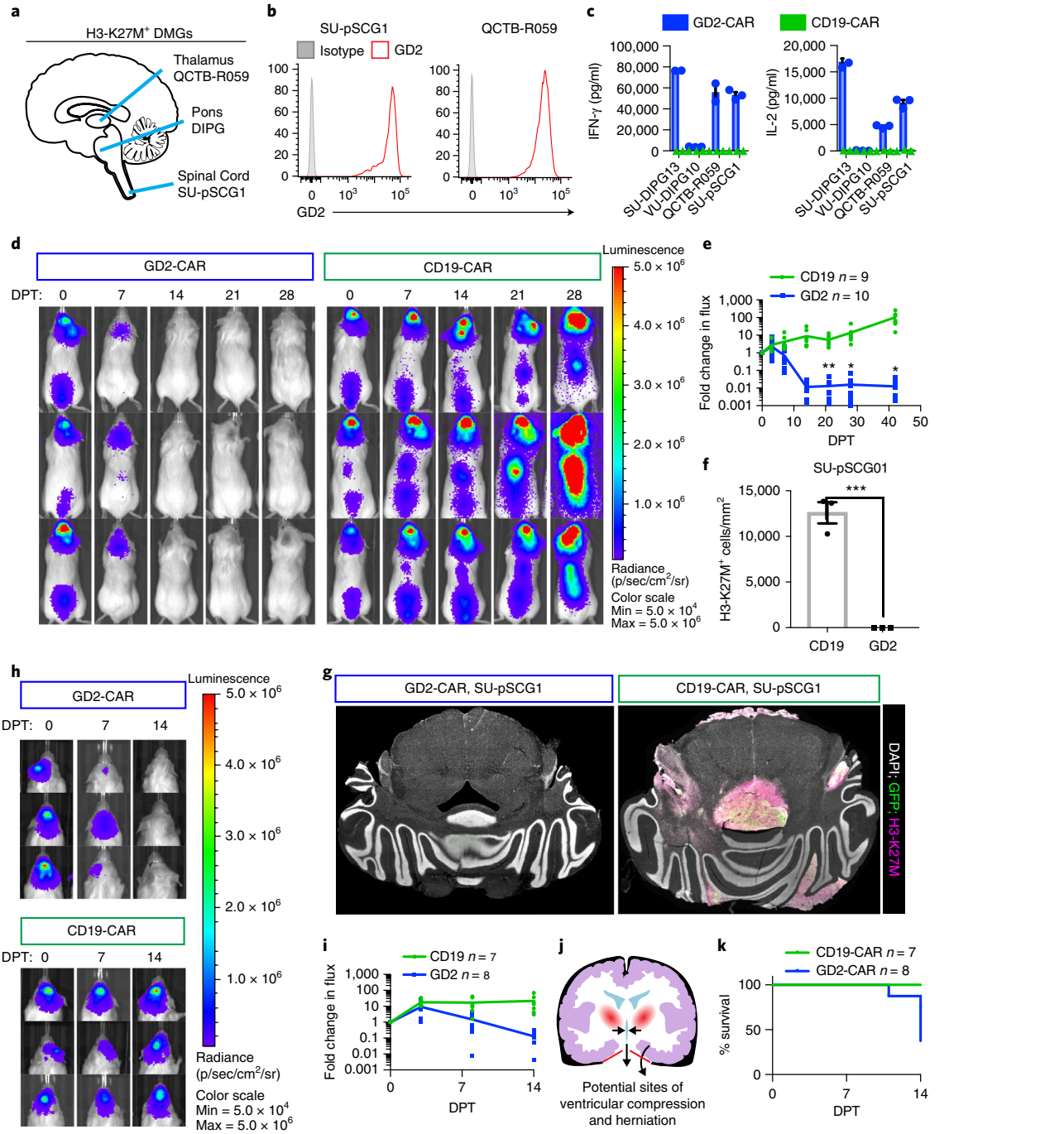

Fig. 4 | GD2 CAR T cell therapy effectively clears other midline H3-K27M-mutant pediatric DMGs but is associated with toxicity in thalamic xenografts. **a**, Anatomic sites of origin of H3-K27M+ DMGs and associated patient-derived cell cultures. **b**, Patient-derived culture models of H3-K27M-mutant tumors that arose in the spinal cord (SU-pSCG1; left) thalamus (QCTB-R059; right) highly and uniformly expressed GD2 as assessed through flow cytometry. **c**, Antigen-dependent secretion of IFN-γ (left) and IL-2 (right) was induced when cultures were incubated with GD2-CAR T cells, but not CD19-CAR T cells, in vitro. **d**, SU-pSCG1 cells stably transduced to express GFP and luciferase were engrafted into the medulla of NSG mice and treated with intravenous infusion of 1×10^7 GD2-CAR T cells ($n=10$ mice) or CD19-CAR T cells ($n=9$ mice), and substantial clearance of engrafted tumor was observed by 14 DPT. Each row represents one mouse over time. **e**, Tumor burden of mice in **d** over time expressed as fold change in flux. **f**, Quantification of H3-K27M+ cells remaining in SU-pSCG1 xenografts at study endpoint revealed near complete clearance of engrafted tumor in GD2-CAR T cell–treated mice ($n=3$ mice) compared to CD19-CAR T cell–treated controls ($n=3$ mice). **g**, Tiled immunofluorescence images of GFP+H3-K27M+ glioma cells across affected regions. **h**, Tumor burden assessed through bioluminescence imaging in NSG mice orthotopically engrafted with the H3-K27M-mutant patient-derived cell culture QCTB-R059 into the thalamus that were treated with systemic administration of GD2-CAR T cells ($n=8$ mice) or CD19-CAR T cells ($n=7$ mice) as described for SU-pSCG1. **i**, Tumor burden of mice in **h** over time expressed as fold change in flux. **j**, Diagram showing the risk for third ventricular compression and herniation through the tentorium cerebelli (red) accompanying inflammation in the thalamus. **k**, GD2-CAR T cell therapy–associated deaths in mice with QCTB-R059 thalamic xenografts observed by 14 DPT highlight the hazards of immunotherapy for midline tumors ($n=8$ GD2-CAR T cell– and 7 CD19-CAR T cell–treated mice). Data are shown as mean ± s.e.m. $^{***}P<0.001$, $^{*}P<0.05$ by unpaired two-tailed Student's *t*-test with Holm–Sidak correction for multiple comparisons, $n=3$ independent samples for in vitro cytokine experiments. Experiments in **b**, **c**, **e**, **f** and **g** were replicated twice.

neuroinflammation in neuroanatomical locations intolerant of swelling. The thalamus—located just above the cerebellar tentorial notch—is a precarious location for edema, particularly when already expanded by tumor, and swelling in this location can precipitate hydrocephalus from third ventricular compression, increased intracranial pressure and lethal transtentorial herniation (Fig. 4j). Meticulous clinical monitoring and neurointensive management of edema will be required for successful clinical translation of this powerful immunotherapy, particularly for thalamic tumors; however, this may be insufficient to mitigate the peril of neuroinflammation at midline brain locations susceptible to herniation.

Although stark tumor clearance occurs in these xenograft models, the persistence of small numbers of tumor cells that are negative for GD2 expression by immunofluorescence staining suggests that multimodal therapy could be required to circumvent potential antigen escape (Supplementary Fig. 4). Although GD2 antibody-associated neuropathy has been observed in clinical trials, it is critical to note that in trials to date using GD2-CAR T cells, in which the targeting domain is derived from the same antibody as used here, treatment-associated neuropathy was not been observed[15–17]. The effects of robust T cell infiltration and potent killing with associated inflammation within the tumor site represents a CNS-tumor-specific element of the larger category of possible neurotoxic complications of CAR T cell therapy, distinct from the observed CAR T cell therapy–associated encephalopathy syndrome (CRES) that occurs in the context of cytokine release and appears to result from endothelial dysfunction[39]. The importance of careful monitoring for hydrocephalus and signs of increased intracranial pressure cannot be overemphasized and will require careful inpatient monitoring with frequent neurological and fundoscopic exams and neuroimaging as indicated. Neurosurgical interventions, such as intraventricular shunt placement for relief of hydrocephalus or even craniectomy for decompression, may be required to support children through the phase of tumoricidal neuroinflammation.

In summary, we have identified GD2 as a newly discovered immunotherapy target in H3-K27M-mutant DMGs and have demonstrated potent antitumor efficacy of GD2-CAR T cells delivered systemically in five independent patient-derived orthotopic xenograft models representing three distinct H3-K27M-mutant glioma subtypes of pons, thalamus and spinal cord. Upregulation of genes encoding ganglioside synthesis pathway components in H3-K27M-mutant pediatric high-grade gliomas relative to H3-WT pediatric high-grade gliomas suggests that this mutant histone drives GD2 overexpression. Tumor-associated inflammation generated through CAR T cell activity is tolerated by the majority of mice in this setting, suggesting the possibility for a therapeutic window with neurointensive management despite the precarious anatomic sites of these midline tumors, but putative tolerability of this approach remains to be demonstrated in children with H3-K27M$^+$ DMG. If the results in mouse models are predictive of results in humans, this immunotherapeutic strategy could be transformative for the outcomes of children with H3-K27M-mutant DMGs.

Methods

Methods, including statements of data availability and any associated accession codes and references, are available at https://doi.org/10.1038/s41591-018-0006-x.

Received: 5 June 2017; Accepted: 31 January 2018;
Published online: 16 April 2018

References

1. Paugh, B. S. et al. Novel oncogenic PDGFRA mutations in pediatric high-grade gliomas. *Cancer Res.* **73**, 6219–6229 (2013).
2. Wu, G. et al. Somatic histone H3 alterations in pediatric diffuse intrinsic pontine gliomas and non-brainstem glioblastomas. *Nat. Genet.* **44**, 251–253 (2012).
3. Buczkowicz, P. et al. Genomic analysis of diffuse intrinsic pontine gliomas identifies three molecular subgroups and recurrent activating ACVR1 mutations. *Nat. Genet.* **46**, 451–456 (2014).
4. Taylor, K. R. et al. Recurrent activating ACVR1 mutations in diffuse intrinsic pontine glioma. *Nat. Genet.* **46**, 457–461 (2014).
5. Wu, G. et al. The genomic landscape of diffuse intrinsic pontine glioma and pediatric non-brainstem high-grade glioma. *Nat. Genet.* **46**, 444–450 (2014).
6. Jones, C. et al. Pediatric high-grade glioma: biologically and clinically in need of new thinking. *Neuro Oncol.* **19**, 153–161 (2016).
7. Lee, D. W. et al. T cells expressing CD19 chimeric antigen receptors for acute lymphoblastic leukaemia in children and young adults: a phase 1 dose-escalation trial. *Lancet* **385**, 517–528 (2015).
8. Davila, M. L. et al. Efficacy and toxicity management of 19-28z CAR T cell therapy in B cell acute lymphoblastic leukemia. *Sci. Transl. Med.* **6**, 224ra25 (2014).
9. Maude, S. L. et al. Chimeric antigen receptor T cells for sustained remissions in leukemia. *N. Engl. J. Med.* **371**, 1507–1517 (2014).
10. Gardner, R. A. et al. Intent-to-treat leukemia remission by CD19 CAR T cells of defined formulation and dose in children and young adults. *Blood* **129**, 3322–3331 (2017).
11. Brown, C. E. et al. Regression of glioblastoma after chimeric antigen receptor T-cell therapy. *N. Engl. J. Med.* **375**, 2561–2569 (2016).
12. Ahmed, N. et al. HER2-specific chimeric antigen receptor-modified virus-specific T cells for progressive glioblastoma: a phase 1 dose-escalation Trial. *JAMA Oncol.* **3**, 1094–1101 (2017).
13. O'Rourke, D.M. et al. A single dose of peripherally infused EGFRvIII-directed CAR T cells mediates antigen loss and induces adaptive resistance in patients with recurrent glioblastoma. *Sci. Transl. Med.* **9**, eaaa0984 (2017).
14. Long, A. H. et al. 4-1BB costimulation ameliorates T cell exhaustion induced by tonic signaling of chimeric antigen receptors. *Nat. Med.* **21**, 581–590 (2015).
15. Pule, M. A. et al. Virus-specific T cells engineered to coexpress tumor-specific receptors: persistence and antitumor activity in individuals with neuroblastoma. *Nat. Med.* **14**, 1264–1270 (2008).
16. Louis, C. U. et al. Antitumor activity and long-term fate of chimeric antigen receptor-positive T cells in patients with neuroblastoma. *Blood* **118**, 6050–6056 (2011).
17. Heczey, A. et al. CAR T cells administered in combination with lymphodepletion and PD-1 inhibition to patients with neuroblastoma. *Mol. Ther.* **25**, 2214–2224 (2017).
18. Majzner, R. G., Heitzeneder, S. & Mackall, C. L. Harnessing the immunotherapy revolution for the treatment of childhood cancers. *Cancer Cell* **31**, 476–485 (2017).
19. Khuong-Quang, D. A. et al. K27M mutation in histone H3.3 defines clinically and biologically distinct subgroups of pediatric diffuse intrinsic pontine gliomas. *Acta Neuropathol.* **124**, 439–447 (2012).
20. Schwartzentruber, J. et al. Driver mutations in histone H3.3 and chromatin remodelling genes in paediatric glioblastoma. *Nature* **482**, 226–231 (2012).
21. Thomas, S., Straathof, K., Himoudi, N., Anderson, J. & Pule, M. An optimized GD2-targeting retroviral cassette for more potent and safer cellular therapy of neuroblastoma and other cancers. *PLoS One* **11**, e0152196 (2016).
22. Long, A. H. et al. Reduction of MDSCs with all-trans retinoic acid improves CAR therapy efficacy for sarcomas. *Cancer Immunol. Res.* **4**, 869–880 (2016).
23. Yu, A. L. et al. Anti-GD2 antibody with GM-CSF, interleukin-2, and isotretinoin for neuroblastoma. *N. Engl. J. Med.* **363**, 1324–1334 (2010).
24. Perez Horta, Z., Goldberg, J. L. & Sondel, P. M. Anti-GD2 mAbs and next-generation mAb-based agents for cancer therapy. *Immunotherapy* **8**, 1097–1117 (2016).
25. Hong, J. J. et al. Successful treatment of melanoma brain metastases with adoptive cell therapy. *Clin. Cancer Res.* **16**, 4892–4898 (2010).
26. Suzuki, K. The pattern of mammalian brain gangliosides. II. Evaluation of the extraction procedures, postmortem changes and the effect of formalin preservation. *J. Neurochem.* **12**, 629–638 (1965).
27. Kramer, K. et al. Compartmental intrathecal radioimmunotherapy: results for treatment for metastatic CNS neuroblastoma. *J. Neurooncol.* **97**, 409–418 (2010).
28. Kramer, K. et al. A phase II study of radioimmunotherapy with intraventricular 131 I-3F8 for medulloblastoma. *Pediatr. Blood Cancer* **65**, e26754 (2018).
29. Monje, M. et al. Hedgehog-responsive candidate cell of origin for diffuse intrinsic pontine glioma. *Proc. Natl Acad. Sci. USA* **108**, 4453–4458 (2011).
30. Qin, E. Y. et al. Neural precursor-derived pleiotrophin mediates subventricular zone invasion by glioma. *Cell* **170**, 845–859 (2017).
31. Grasso, C. S. et al. Functionally defined therapeutic targets in diffuse intrinsic pontine glioma. *Nat. Med.* **21**, 555–559 (2015).
32. Fry, T. J. et al. CD22-targeted CAR T cells induce remission in B-ALL that is naive or resistant to CD19-targeted CAR immunotherapy. *Nat. Med.* **24**, 20–28 (2018).

33. Walker, A. J. et al. Tumor antigen and receptor densities regulate efficacy of a chimeric antigen receptor targeting anaplastic lymphoma kinase. *Mol. Ther.* **25**, 2189–2201 (2017).
34. Ali, N. et al. Xenogeneic graft-versus-host-disease in NOD-scid IL-2Rγnull mice display a T-effector memory phenotype. *PLoS One* **7**, e44219 (2012).
35. Nagaraja, S. et al. Transcriptional dependencies in diffuse intrinsic pontine glioma. *Cancer Cell* **31**, 635–652 (2017).
36. Louveau, A. et al. Structural and functional features of central nervous system lymphatic vessels. *Nature* **523**, 337–341 (2015).
37. Louis, D. N. et al. The 2016 World Health Organization classification of tumors of the central nervous system: a summary. *Acta Neuropathol.* **131**, 803–820 (2016).
38. Wolchok, J. D. et al. Guidelines for the evaluation of immune therapy activity in solid tumors: immune-related response criteria. *Clin. Cancer Res.* **15**, 7412–7420 (2009).
39. Gust, J. et al. Endothelial activation and blood–brain barrier disruption in neurotoxicity after adoptive immunotherapy with CD19 CAR-T cells. *Cancer Discov.* **7**, 1404–1419 (2017).

Acknowledgements

We thank the following for generously providing cell cultures: A. Moore (University of Queensland) and C. Jones (Institute of Cancer Research) for QCTB R059, R. Seeger (Children's Hospital Los Angeles) for CHLA136, 255, C. Khanna (National Cancer Institute) for MG63-3 and L. Helman (Children's Hospital Los Angeles) for EW8 and TC32.

This work was supported by a Stand Up To Cancer–St. Baldrick's–National Cancer Institute Pediatric Dream Team Translational Cancer Research Grant (C.L.M.). Stand Up To Cancer is a program of the Entertainment Industry Foundation administered by the American Association for Cancer Research. C.L.M is a member of the Parker Institute for Cancer Immunotherapy, which supports the Stanford University Cancer Immunotherapy Program. The authors gratefully acknowledge support from the National Institute of Neurological Disorders and Stroke (F31NS098554 to C.W.M. and R01NS092597 to M.M.), Abbie's Army Foundation (M.M.), Unravel Pediatric Cancer (M.M.), Maiy's Miracle Foundation (E.P.A.), Stella S. Jones Foundation (M.M.), McKenna Claire Foundation (M.M.), Alex's Lemonade Stand Foundation (M.M.), Izzy's Infantry Foundation (M.M.), The Cure Starts Now Foundation and DIPG Collaborative (M.M.), Lyla Nsouli Foundation (M.M.), Declan Gloster Memorial Fund (M.M.), N8 Foundation (M.M.), Fly a Kite Foundation (M.M.), Liwei Wang Research Fund (M.M.), Virginia and D.K. Ludwig Fund for Cancer Research (M.M. and C.L.M.), Sam Jeffers Foundation (M.M.), Michael Mosier DEFEAT DIPG Foundation (M.M.), ChadTough Foundation (M.M.), Reller Family Research Fund, Child Health Research Institute at Stanford and SPARK program (M.M.) and the Anne T. and Robert M. Bass Endowed Faculty Scholarship in Pediatric Cancer and Blood Diseases (M.M.).

Author contributions

C.W.M. and E.P.A. performed the antibody array screening. C.W.M. and M.M. identified GD2 as a target in H3-K27M$^+$ DMGs. C.W.M. and S.S. performed immunohistochemistry and immunofluorescence microscopy on primary and xenograft tissue. L.L. and R.G.M. designed CAR constructs. R.G.M. and M.K. prepared CAR T cells for in vivo experiments. C.W.M. and P.J.W. conducted in vivo experiments. R.G.M., M.K. and S.P.R. performed in vitro T cell experiments and flow cytometry. E.H. contributed VUMC-DIPG10 and data on ganglioside synthesis pathway expression. H.V. performed neuropathological review of brain tissue. S.H. performed CRISPR–Cas9-mediated gene editing. C.W.M., R.G.M., H.V., M.M. and C.L.M. contributed to data analysis and interpretation. C.W.M., M.M., R.G.M. and C.L.M wrote the manuscript. C.W.M. and R.G.M. made the figures. M.M. and C.L.M. supervised all aspects of the work.

Competing interests

C.L.M, M.M., R.G.M. and C.W.M. are inventors on a patent application for GD2-directed CAR use for H3-K27M DMG.

Additional information

Supplementary information is available for this paper at https://doi.org/10.1038/s41591-018-0006-x.

Reprints and permissions information is available at www.nature.com/reprints.

Correspondence and requests for materials should be addressed to M.M. or C.L.M.

Publisher's note: Springer Nature remains neutral with regard to jurisdictional claims in published maps and institutional affiliations.

Methods

DMG cultures. Patient-derived glioma cell cultures were generated as previously described[40]. Briefly, tumor tissue was dissociated mechanically and enzymatically (Liberase DH, Roche) before separation of myelin and debris through sucrose centrifugation. Neurosphere-generating cultures were maintained in serum-free medium supplemented with B27 (ThermoFisher), epidermal growth factor (EGF), fibroblast growth factor (FGF), platelet-derived growth factor (PDGF)-AA, PDGF-BB (Shenandoah Biotechnology) and Heparin (StemCell Technologies). All cultures were validated and monitored through short tandem repeat (STR) fingerprinting (Supplementary Table 2) and were verified to be mycoplasma-free within the previous 6 months (MycoAlert Plus, Lonza). SU-DIPG6 and SU-DIPG13 have been previously referred to as and are identical to SU-DIPG-VI and SU-DIPG-XIII, respectively. Clinical characteristics and STR fingerprints of all DIPG and pSCG cultures[30] along with the QCTB-R059 culture[4] used here have been previously reported. For all studies using human tissue, written informed consent was obtained per guidelines of the approved Stanford Institutional Review Board protocol.

Cell surface screening. Cell surface markers present on DIPG cell cultures were screened using a panel of monoclonal antibodies against human cell surface markers (Lyoplate, BD Biosciences). Low-passage (<12) DIPG cultures from tumor tissue collected at autopsy were expanded in serum-free, neurosphere-forming conditions[40] and were allotted to 96-well plates and blocked with 1 µg of goat IgG per million cells to reduce nonspecific binding of the secondary antibodies subsequently used in the assay. Cells were then incubated sequentially with primary and secondary antibodies with intermediate wash steps according to the manufacturer's instructions. Dead cells were then labeled with a LIVE–DEAD violet stain (ThermoFisher), and following washes, cells were fixed in 1% PFA for 10 min at room temperature. The following day, stained cells were analyzed using flow cytometry. Doublets and dead cells were excluded through gating, and the mean fluorescence intensity of antibody labeling for each target on the panel was normalized to the mean fluorescence intensity for the matched isotype control, per the manufacturer's recommendations.

Immunohistochemistry and light microscopy. Primary tumor samples from patients with DIPG were fixed overnight in 4% paraformaldehyde–PBS, and then transferred to 30% sucrose until the tissue samples sank (2–3 d). Tissues were then transferred to cryomolds and embedded in optimal-cutting temperature (OCT) compound (TissueTek). 10-µm cryosections were generated on a cryostat (Leica), and endogenous peroxidase activity was neutralized (Bloxall, Vector Laboratories) before permeabilization (0.3% Triton X-100, TBS) and blocking (5% horse serum, Vector Laboratories). Sequential double-staining immunohistochemistry was conducted for H3-K27M (Abcam ab190631, 1:1,000, 1 h RT) and GD2 (14g2a, BD, 1:500, 1 h at RT). H3-K27M was developed with a peroxidase secondary (ImmPRESS VR anti–rabbit IgG, Vector Laboratories, 30 min at RT) and DAB substrate (BD). Under these conditions, H3-K27M$^+$ cells could be routinely identified in multiple tissues confirmed to bear both *H3F3A* and *HISTH1B3* mutations as determined through Sanger sequencing, but staining was absent in tissues from non-DIPG tumor samples confirmed to be H3-WT through Sanger sequencing. After quenching the DAB substrate development in Tris-buffered saline (TBS) and staining with the 14g2a primary antibody, GD2 signal was developed using a polymer-based alkaline phosphatase secondary antibody (ImmPRESS AP anti–mouse IgG, Vector Laboratories, 30 min at RT) and blue alkaline phosphatase substrate (Vector Blue AP substrate kit, Vector Laboratories, 150 s at RT). Alkaline phosphatase development was quenched in TBS, and samples were mounted and imaged (Zeiss AxioObserver). For H&E staining, mice were deeply anesthetized through intraperitoneal injection of tribromoethanol and were perfused transcardially with cold PBS. Their brains were removed and fixed overnight in 4% paraformaldehyde–PBS. The brains were then transferred to 70% ethanol and subsequently embedded in paraffin, sectioned and stained with H&E. H&E histology was analyzed by an expert neuropathologist (H.V.).

Immunofluorescence and confocal microscopy. Mice were deeply anesthetized with tribromoethanol (Avertin) before being perfused transcardially with cold PBS. Brains were then removed and fixed overnight in 4% PFA–PBS before being transferred to 30% sucrose and were allowed to sink (2–3 d). Serial 40-µm coronal sections were then cut on a freezing microtome and floated in a tissue cryoprotectant solution (glycerol, ethylene glycol, phosphate buffer) before storage at −20 °C. Serial sections were then stained overnight at 4 °C. The primary antibodies that were used were: rabbit anti-H3-K27M (Abcam, 1:1,000), rabbit anti–cleaved caspase-3 (Cell Signaling Technology, 9661, 1:250), mouse anti-NeuN (Millipore, MAB377, 1:500) and rabbit anti-IBA1 (Wako, 019-19741, 1:500). Secondary antibodies conjugated with AlexaFluor 594 or 647 were used at 4 °C overnight to detect primary labeling (Jackson ImmunoResearch, 711-605-152, 715-585-151, 1:500). Mounted samples were imaged using confocal microscopy (Zeiss LSM710), and acquired Z stacks through the tumor region were flattened through maximum intensity projection (ImageJ). To quantify tumor-cell density, cells within the borders of infiltrating tumor in acquired micrographs were counted and normalized to the tumor area (ImageJ), and the sum of all cells was normalized to the total area investigated across three or four sections for each mouse in a 1:12 series.

RT–qPCR. Cultures were plated in triplicate under standard growth conditions and harvested in TRIzol 24 h later. After DNase treatment, extracted RNA was reverse transcribed (Maxima first strand, ThermoFisher) and used as template for qPCR reactions (Maxima SYBR green, ThermoFisher). The primers used are listed in Supplementary Table 3. No-template and no-reverse-transcriptase controls did not substantially amplify. For each of the triplicate cultures, technical duplicates were assayed and averaged. Relative expression was then calculated using the ΔΔCT method.

CAR construction, retroviral vector production and T cell transduction. The GD2-CAR incorporates the single-chain variable fragment derived from the 14g2a monoclonal antibody, a CD8 transmembrane domain and 4-1BB and T cell receptor ζ signaling endodomains. The CD19-CAR was similarly configured but incorporated the FMC63 single-chain variable fragment. The GD2-4-1BBz and CD19-4-1BBz CAR retroviral vectors were constructed as previously described[41]. GD2-4-1BBz CAR– and CD19-4-1BBz CAR–encoding retroviral supernatants were produced via transient transfection of the 293GP cell line, as previously described[42]. Briefly, 293GP cells were transfected on poly-D-lysine-coated plates via Lipofectamine 2000 (Life Technologies) with the plasmids encoding the CARs and the RD114 envelope protein. Supernatants were collected 48 h and 72 h after transfection. Isolated human T cells were activated with anti-CD3 and anti-CD28 beads (Life Technologies) in a 3:1 bead:cell ratio with 40 IU/ml IL-2 for 3 d. Activated T cells were then retrovirally transduced on days 3 and 4 as described[14] using Retronectin (Takara)–coated plates and cultured in 300 IU/ml IL-2. Anti-CD3 and anti-CD28 beads were removed on day 5, and medium and IL-2 were changed every 2–3 d. Flow cytometry using the 1A7 anti-idiotype antibody (National Cancer Institute BRB Repository)[43] for the GD2-4-1BBz CAR and 136.20.1, an FMC63 anti-idiotype antibody[44], or Protein L (Pierce) for the CD19-4-1BBz CAR was used to assess transduction efficiency for each batch of CAR T cells.

In vitro cytokine generation and cell killing. In vitro cell killing activity of GD2 and CD19-CAR T cells was assessed with a luciferase-based assay as previously described[41]. Tumor cells lentivirally transduced to stably express firefly luciferase (10,000 tumor cells per well) were co-incubated with GD2 or CD19-CAR T-cells for 24 h at effector-to-target (E:T) ratios ranging from 10:1 to 2.5:1. The Steady-Glo Luciferase Assay System (Promega) was used to measure residual luciferase activity from remaining tumor target cells, and lysis was calculated as follows: percent lysis = 100 − (((average signal from T cell–treated wells) / (average signal from untreated target wells)) × 100).

Cytokine production by CAR T cells in vitro was evaluated through co-incubation of CAR$^+$ T cells with target tumor cells at a 1:1 ratio (100,000 cells each), and CAR$^+$ T cell counts incorporated the transduction efficiency as assessed through anti-idiotype staining and flow cytometry. The total number of T cells used for the control CD19-4-1BBz CAR T cells matched the number used for the GD2-4-1BBz CAR T cells to ensure that the total number of T cells remained consistent across groups. After 24 h, supernatants were harvested, and cytokine levels were measured using ELISA for IL-2 and IFN-γ (BioLegend).

T cell proliferation. GD2-CAR T cells on Day 15 of culture were labeled with Cell Trace Violet (ThermoFisher) according to the manufacturer's protocol. Labeled GD2-CAR T cells were either incubated with no tumor, VUMC-DIPG10 (GD2$^-$H3-K27M$^-$) or SU-DIPG13 (GD2$^+$H3-K27M$^+$). After 5 d of incubation, cells were collected and analyzed for proliferation using flow cytometry. Analysis was performed on only CAR$^+$ T cells identified through anti-idiotype staining.

Orthotopic xenograft generation and treatment. Orthotopic DIPG xenografts were generated as previously described[31]. All in vivo experiments were approved by the Stanford University Institutional Care and Use Committee and were performed in accordance with institutional guidelines. Mice were housed according to institutional guidelines with free access to food and water on a 12-h light–dark cycle. Briefly, patient-derived DIPG cell cultures (SU-DIPG6 and SU-DIPG13-FL) previously transduced with a lentivirus expressing eGFP and firefly luciferase driven by the cytomegalovirus (CMV) promoter were infused via stereotaxic injector (Stoelting) into the pons (coordinates from lambda: anterior/posterior (A/P), −3 mm; dorsal/ventral (D/V) −3 mm; 100,000 cells) of cold-anesthetized newborn (postnatal day 0–2) NOD-*scid* IL2rg$^{-/-}$ (NSG) mice (Jax). Orthotopic pediatric glioma xenografts in the spinal cords of the mice were generated through stereotaxic injection of SU-pSCG1 transduced with a lentivirus expressing eGFP and firefly luciferase driven by the CAG promoter into the medulla of isoflurane-anesthetized P35 NSG mice (coordinates from lambda: medial/lateral (M/L), +0.7 mm; A/P, −3.5 mm; D/V, −4.5 mm; 600,000 cells). Orthotopic thalamic glioma xenografts were generated through stereotaxic injection of QCTB-R059 transduced with a lentivirus expressing eGFP and firefly luciferase driven by the CMV promoter into the thalamus of isoflurane-anesthetized P35 NSG mice (coordinates from bregma: M/L, +0.8 mm; A/P −1 mm; D/V −3.5 mm; 600,000 cells). Tumors

were then allowed to develop for 60 d. Prior to treatment, tumor burden was assessed through in vivo luminescence imaging (IVIS Spectrum, PerkinElmer), and total flux was calculated using the included software (Living Image, Perkin Elmer) as the radiance through standard circular regions of interest (ROIs) centered on the mouse's head. Paired background regions were quantified using circular ROIs over the mouse's flank, where no substantial luminescence was detected above background. Mice were rank-ordered according to tumor burden and distributed sequentially into GD2-CAR T cell or CD19-CAR T cell treatment groups such that populations with equivalent initial tumor burden underwent each arm of therapy. Initial burden assessed in this manner was equivalent across treatment groups and engrafted cell lines (Supplementary Fig. 3). SU-DIPG13P* cells were injected into the pons of isoflurane-anesthetized P35 NSG mice (coordinates from lambda: M/L, +1 mm; A/P, −0.8 mm; D/V, −5 mm; 600,000 cells) and were allowed to develop for 14 d before T cell administration. CAR T cells were delivered in a concentration of 1×10^7 transduced cells in 200 µl of PBS (assessed through idiotype staining using flow cytometry, routinely > 60%) through intravenous injection into the tail veins of mice. For cases in which transduction efficiencies varied between GD2-CAR T cells and CD19-CAR T cells, the concentration of CD19-CAR T cells was adjusted to match the total dose of human T cells present in the GD2-CAR T cell infusion. Tumor burden was monitored longitudinally through in vivo luminescence imaging. Owing to the obvious nature of GD2-CAR T cell response, blinding in initial cohorts was deemed ineffective and subsequently not performed. All images were scaled to display minimum flux intensity as 5×10^4 and maximum as 5×10^6, and then images from individual mice were arranged with like-treated mice in the cohort for display in figures. Trial endpoint at 50 DPT was determined in the first three cohorts; at this point, mice in both GD2-CAR T cell and CD19-CAR T cell treatment groups had substantial hair loss, reduced activity and weight loss, which constituted morbidity criteria for euthanasia.

CRISPR–Cas9-mediated deletion of the GD2 synthase gene. Deletion of the gene encoding GD2 synthase (*B4GALNT1*) in SU-DIPG13 cells was accomplished through electroporation of DIPG13 with Cas9–sgRNA ribonucleoprotein complexes as previously described[45]. Briefly, guide RNAs (gRNAs) targeting exon 1 of *B4GALNT1* (5′-CGUCCCGGGUGCUCGCGUAC-3′ and 5′ -CCGGCUACCUCUUGCGCCGU-3′, Synthego) were incubated with Cas9 nuclease to form ribonucleoprotein complexes, which were electroporated with an Amaxa 4-D nucleofector (SEM Buffer, program DS-112). In parallel, a control gRNA targeting the AAVS1 locus[46] (5′-GGGGCCACUAGGGACAGGAU-3′) was electroporated with Cas9 nuclease as a ribonucleoprotein complex using identical parameters. GD2$^-$ cells electroporated with *B4GALNT1*-targeting gRNAs were isolated through FACS sorting, and deletion was confirmed using Sanger sequencing and tracking of indels by decomposition (TIDE) analysis[47].

Statistics and reproducibility. Statistical tests were conducted using Prism (GraphPad) software unless otherwise indicated. A Gaussian distribution was confirmed using the Shapiro–Wilk normality test. For parametric data, unpaired, two-tailed Student's *t*-tests and one-way ANOVA with Tukey's post hoc tests to further examine pairwise differences were used. For survival analysis, a log-rank (Mantel–Cox) test was used. A level of $P < 0.05$ was used to designate significant differences. On the basis of the variance of xenograft growth in control mice, we used at least three mice per treatment group to give 80% power to detect an effect size of 20% with a significance level of 0.05. For all mouse experiments, the number of independent mice used is listed in the figure legend. For each of the five patient-derived xenograft models used, at least two independent cohorts were tested (i.e., independent litters of mice on different days with independent batches of cells). For cytokine and in vitro cell killing experiments, $n = 3$ wells, and experiments were repeated twice.

Reporting Summary. Further information on experimental design is available in the Nature Research Reporting Summary linked to this article.

Data availability. The datasets generated during the current study are available from the corresponding author upon reasonable request.

References

40. Lin, G. L. & Monje, M. A protocol for rapid post-mortem cell culture of diffuse intrinsic pontine glioma (DIPG). *J. Vis. Exp.* **7**, e55360 (2017).
41. Lynn, R. C. et al. Targeting of folate receptor β on acute myeloid leukemia blasts with chimeric antigen receptor-expressing T cells. *Blood* **125**, 3466–3476 (2015).
42. Haso, W. et al. Anti-CD22-chimeric antigen receptors targeting B-cell precursor acute lymphoblastic leukemia. *Blood* **121**, 1165–1174 (2013).
43. Sen, G., Chakraborty, M., Foon, K. A., Reisfeld, R. A. & Bhattacharya-Chatterjee, M. B. Induction of IgG antibodies by an anti-idiotype antibody mimicking disialoganglioside GD2. *J. Immunother.* **21**, 75–83 (1998).
44. Jena, B. et al. Chimeric antigen receptor (CAR)-specific monoclonal antibody to detect CD19-specific T cells in clinical trials. *PLoS One* **8**, e57838 (2013).
45. Hendel, A. et al. Chemically modified guide RNAs enhance CRISPR-Cas genome editing in human primary cells. *Nat. Biotechnol.* **33**, 985–989 (2015).
46. Chu, V. T. et al. Increasing the efficiency of homology-directed repair for CRISPR–Cas9-induced precise gene editing in mammalian cells. *Nat. Biotechnol.* **33**, 543–548 (2015).
47. Brinkman, E. K., Chen, T., Amendola, M. & van Steensel, B. Easy quantitative assessment of genome editing by sequence trace decomposition. *Nucleic Acids Res.* **42**, e168 (2014).

nature research

Corresponding author(s): Michelle Monje, Crystal Mackall

Life Sciences Reporting Summary

Nature Research wishes to improve the reproducibility of the work that we publish. This form is intended for publication with all accepted life science papers and provides structure for consistency and transparency in reporting. Every life science submission will use this form; some list items might not apply to an individual manuscript, but all fields must be completed for clarity.

For further information on the points included in this form, see Reporting Life Sciences Research. For further information on Nature Research policies, including our data availability policy, see Authors & Referees and the Editorial Policy Checklist.

Please do not complete any field with "not applicable" or n/a. Refer to the help text for what text to use if an item is not relevant to your study.
For final submission: please carefully check your responses for accuracy; you will not be able to make changes later.

Experimental design

1. Sample size

   Describe how sample size was determined.

   Based on the variance of xenograft growth in control mice, power calculations indicated use of at least 3 mice per genotype to give 80% power to detect an effect size of 20% with a significance level of 0.05. For all animal studies, 2 or more independent cohorts were included with n=3 or more animals per treatment group

2. Data exclusions

   Describe any data exclusions.

   (Fig 4e) A single CD19-CAR control animal with tumor flux much larger than matched animals of the cohort (identified as an outlier, GraphPad Prism ROUT method, Q=1%), was excluded from statistical analysis.

3. Replication

   Describe the measures taken to verify the reproducibility of the experimental findings.

   All experiments were reproduced a minimum of 2 times, and attempts at replication were successful.

4. Randomization

   Describe how samples/organisms/participants were allocated into experimental groups.

   For animal studies utilizing luciferase-expressing cell lines, animals were rank-ordered by initial tumor flux and sequentially randomized to GD2 or CD19 CAR T cell treatment groups. For survival cohorts lacking luciferase expression, animals were randomized into GD2 or CD19 CAR T cell treatment groups.

5. Blinding

   Describe whether the investigators were blinded to group allocation during data collection and/or analysis.

   Investigators were initially blinded to treatment in initial cohorts, but the dramatic nature of GD2 response renders blinding ineffective upon tumor clearance. For all microscopy analysis, investigators were blinded to treatment group during cell counting.

Note: all in vivo studies must report how sample size was determined and whether blinding and randomization were used.

6. Statistical parameters

For all figures and tables that use statistical methods, confirm that the following items are present in relevant figure legends (or in the Methods section if additional space is needed).

n/a	Confirmed
☐	☒ The exact sample size (*n*) for each experimental group/condition, given as a discrete number and unit of measurement (animals, litters, cultures, etc.)
☐	☒ A description of how samples were collected, noting whether measurements were taken from distinct samples or whether the same sample was measured repeatedly
☐	☒ A statement indicating how many times each experiment was replicated
☐	☒ The statistical test(s) used and whether they are one- or two-sided *Only common tests should be described solely by name; describe more complex techniques in the Methods section.*
☐	☒ A description of any assumptions or corrections, such as an adjustment for multiple comparisons
☐	☒ Test values indicating whether an effect is present *Provide confidence intervals or give results of significance tests (e.g. P values) as exact values whenever appropriate and with effect sizes noted.*
☐	☒ A clear description of statistics including central tendency (e.g. median, mean) and variation (e.g. standard deviation, interquartile range)
☐	☒ Clearly defined error bars in all relevant figure captions (with explicit mention of central tendency and variation)

See the web collection on statistics for biologists for further resources and guidance.

Software

Policy information about availability of computer code

7. Software

Describe the software used to analyze the data in this study.

Statistical tests were conducted using Prism (GraphPad) software for most analyses. For confirmation of Cas9-mediated deletion of GD2 synthase, the TIDE webtool was utilized (version 2.0.1). Microscopy images were processed in Stereoinvestigator (MBF Biosciences) and ImageJ.

For manuscripts utilizing custom algorithms or software that are central to the paper but not yet described in the published literature, software must be made available to editors and reviewers upon request. We strongly encourage code deposition in a community repository (e.g. GitHub). *Nature Methods* guidance for providing algorithms and software for publication provides further information on this topic.

Materials and reagents

Policy information about availability of materials

8. Materials availability

Indicate whether there are restrictions on availability of unique materials or if these materials are only available for distribution by a third party.

Materials including patient-derived cell cultures are freely available with a standard MTA from the corresponding authors.

9. Antibodies

Describe the antibodies used and how they were validated for use in the system under study (i.e. assay and species).

Primary antibodies used were: rabbit anti-H3K27M (Abcam [EPR18340], 1:1000), rabbit polyclonal anti-cleaved caspase-3 (Cell Signaling Technology, 9661, 1:250), mouse anti-NeuN (Millipore, MAB377, 1:500), and rabbit polyclonal Iba1 (Wako, 019-19741, 1:500). Secondary antibodies raised in donkey and conjugated with AlexaFluor 594 or 647 were used at 4C overnight to detect primary labeling (Jackson ImmunoResearch, 1:500).

All antibodies have been validated in the literature and/or in Antibodypedia for use in mouse immunohistochemistry or human cell immunohistochemistry or FACS. To further validate the antibodies on our hands, we confirmed that each antibody stained in the expected cellular patterns and brain-wide distributions.

10. Eukaryotic cell lines

a. State the source of each eukaryotic cell line used.

patient-derived DMG cultures were derived as indicated in the methods and references from primary tumor samples.

b. Describe the method of cell line authentication used.

cell cultures were authenticated by STR fingerprinting

c. Report whether the cell lines were tested for mycoplasma contamination.

Cell cultures are routinely tested for mycoplasma, and all tested negative for mycoplasma

d. If any of the cell lines used are listed in the database of commonly misidentified cell lines maintained by ICLAC, provide a scientific rationale for their use.

no commonly misidentified cell lines were used

Animals and human research participants

Policy information about studies involving animals; when reporting animal research, follow the ARRIVE guidelines

11. Description of research animals

Provide all relevant details on animals and/or animal-derived materials used in the study.

NSG mice were used for all animal studies in the manuscript as indicated in methods section and were housed according to institutional guidelines. Mice of both sexes were used throughout all studies. SU-DIPG6 and SU-DIPG13FL xenografts were established at P0-2 and treated 7-8 weeks later. SU-DIPG13P* were established at P35 and treated 14 days later. SU-pSCG1, and QCTB-R059 xenografts were established at P35 and treated 7-8 weeks later.

Policy information about studies involving human research participants

12. Description of human research participants

Describe the covariate-relevant population characteristics of the human research participants.

This study did not involve human research participants. Covariate characteristics of cell cultures including histone mutation status and sex are provided in Supplementary Table 2.

nature research

Corresponding author(s): Michelle Monje, Crystal Mackall

☐ Initial submission ☐ Revised version ☒ Final submission

Flow Cytometry Reporting Summary

Form fields will expand as needed. Please do not leave fields blank.

Data presentation

For all flow cytometry data, confirm that:

☒ 1. The axis labels state the marker and fluorochrome used (e.g. CD4-FITC).

☒ 2. The axis scales are clearly visible. Include numbers along axes only for bottom left plot of group (a 'group' is an analysis of identical markers).

☒ 3. All plots are contour plots with outliers or pseudocolor plots.

☒ 4. A numerical value for number of cells or percentage (with statistics) is provided.

Methodological details

5. Describe the sample preparation.	Cultured cell lines as indicated were harvested and stained with relevant fluorochome-conjugated antibodies.
6. Identify the instrument used for data collection.	Data were collected on a BD LSR Fortessa analyzer and BD FacsAria II.
7. Describe the software used to collect and analyze the flow cytometry data.	Data were collected in BD FacsDiva and analyzed with FlowJo.
8. Describe the abundance of the relevant cell populations within post-sort fractions.	Surface marker intensity was determined within singlet, live cell fractions as assessed by forward/side scatter and ability to exclude DNA intercalating stain (DAPI). Live cell fractions were routinely >70%.
9. Describe the gating strategy used.	Cell singlets were identified by FSC/SSC gating, and live cells further identified by exclusion of DAPI compared to unstained controls. For cell-surface screens, a fixable live/dead violet stain was used to exclude dead cells. Positive stain intensity was then defined as the median fluorescence intensity (MFI) of the stained population above matched isotype controls as indicated in the methods.

Tick this box to confirm that a figure exemplifying the gating strategy is provided in the Supplementary Information. ☐